Astronomy & Astrophysics manuscript no. Draft-Polaris-v4
January 6, 2016

Magnetic fields and diffuse filaments in the Polaris Flare

M. Berthet[1], F. Levrier[1], P. Hily-Blant[2], E. Falgarone[1], P. Bastien[3], and T. Sousbie[4]

[1] LERMA, Observatoire de Paris, PSL Research University, CNRS, Sorbonne Universités, UPMC, ENS, 24 rue Lhomond, 75231 Paris Cedex 05, France
[2] Université Joseph Fourier / Institut Universitaire de France / IPAG / CNRS, Grenoble, France
[3] Centre de recherche en astrophysique du Québec and Départment de Physique, Université de Montréal, C. P. 6128, Succ. centre-ville, Montréal, QC H3C 3J7, Canada
[4] Institut d'Astrophysique de Paris, CNRS UMR 7095 and UPMC, 98bis, bd Arago, F-75014 Paris, France

Received ...; accepted ...

ABSTRACT

The formation and evolution of filaments play a major role in current models of the early phases of star formation, as signatures of the interplay between gravity, turbulence, and magnetic fields. Studies of starlight polarization combined with *Herschel* maps have in particular exhibited that magnetic fields tend to be parallel to diffuse, non self-gravitating filaments, and perpendicular to more massive ones. We seek to test the former finding in a turbulent and diffuse region of the interstellar medium (ISM), the Polaris Flare, using new starlight polarization data obtained with the "Beauty and the Beast" polarimeter at Mont-Mégantic Observatory. Using this data and IRAS dust emission maps, we present a study of the relative orientations of the magnetic field and filamentary structures of matter observed in the Polaris Flare. We find that the distribution of the angles θ between the sky projected magnetic field and the nearby filaments marginally supports the scenario according to which filaments in the diffuse ISM tend to be aligned with the magnetic field, although the small number of data points available leaves room for deviations in the underlying probability distribution function. This may be a manifestation of a trans-Alfvénic regime in this diffuse, non-starforming molecular cloud.

Key words. ISM: clouds - ISM: magnetic fields - techniques: polarimetric

1. Introduction

Herschel (Pilbratt et al. 2010) and *Planck* (Tauber et al. 2010; Planck Collaboration 2011a) have revealed that the filamentary structure of the interstellar medium (ISM) of the Galaxy, discovered with IRAS, extends to smaller sizes and masses per unit length (Miville-Deschênes et al. 2010; Men'shchikov et al. 2010; Arzoumanian et al. 2011; Planck Collaboration 2011b,c). These filaments are of two types: (1) massive, self-gravitating filaments within which stars are thought to be born through instabilities leading to local gravitational collapse and the formation of prestellar dense cores (André et al. 2014; Planck Collaboration 2011b)[1]; and (2) much more diffuse filaments ("striations") which look like "hair" on the "skin" of the former massive filaments (Chapman et al. 2011; Palmeirim et al. 2013), and are believed to be the loci of the flow of matter from the diffuse medium to denser stuctures. This interpretation is supported by observations of the relative orientation between filaments and the magnetic field. The latter is inferred in the visible and near-infrared from the polarization of light from background stars by aspherical dust grains (Chapman et al. 2011), which tend to align themselves with the local magnetic field (see Planck Collaboration 2015c, and references therein). A counterpart to this polarization is that submillimeter emission from these grains is also polarized, and *Planck* polarization data at 353 GHz has provided the first complete map of this polarized emission (Planck Collaboration 2015a). Observations show an alignment of the magnetic field with striations (Palmeirim et al. 2013), and a change of relative orientation of the magnetic field, from mostly parallel to mostly perpendicular to filamentary structures, as the total gas column density increases above $N_H \sim 10^{22}\,\mathrm{cm}^{-2}$ (Planck Collaboration 2015d). This turnover is precisely what is observed in magnetohydrodynamical (MHD) simulations of the ISM, provided the initial magnetization is large enough (Soler et al. 2013). It is also the column density at which structures are abserved to become gravitationnally supercritical (Crutcher 2012).

This paper presents new polarization data in extinction obtained with the "Beauty and the Beast" polarimeter at Mont-Mégantic Observatory, and aims to use it to establish statistical evidence of the correlation between the orientation of the magnetic field and the orientation of filamentary structures in the field of the Polaris Flare, observed with IRAS. Since the entire field is diffuse, none of these filaments is self-gravitating.The paper is organized as follows : Sect. 2 presents the data used; Sect. 3 presents the method applied on the dust emission map to extract filamentary structures; Sect. 4 gives our main statistical results; Conclusions are summarized in Sect. 5.

2. Observations and data used

2.1. Starlight polarization data

Aspherical, charged, and spinning dust grains in the ISM tend to align with the local magnetic field, through processes such as magnetic relaxation (Davis & Greenstein 1951; Das et al. 2010), mechanical alignment in subsonic gas flows (Lazarian & Hoang 2007), or radiative torques (Hoang et al. 2015, and references therein). Since this alignment is such that the long axis of dust

[1] These self-gravitating filaments harbour sub-structure seen in molecular line emission as a bundle of velocity-coherent fibers (Hacar et al. 2013). Such coherent velocity structures are also seen at much smaller scales (Hily-Blant et al. 2008).

Table 1. Star data : columns give the star's equatorial coordinates (epoch J2000), ID in the Hipparcos and Tycho catalogues, distance, magnitude in the V band, polarization fraction and attached uncertainty, polarization angle and attached uncertainty.

α [h:m:s]	δ [°:′:″]	ID	d [pc]	m_V	p	σ_p	ψ [°]	σ_ψ [°]	α [h:m:s]	δ [°:′:″]	ID	d [pc]	m_V	p	σ_p	ψ [°]	σ_ψ [°]
00:17:40.1	85:00:14.1	1359	180.2	7.8	0.08	0.02	173.3	6.4	00:41:11.1	87:50:42.0	3133	317.0	9.0	0.03	0.05	38	—
00:43:37.0	85:17:07.4	3354	135.0	9.6	0.02	0.02	165	23	00:56:21.2	85:45:00.5	4320	235.3	8.1	0.02	0.03	36	33
01:00:55.7	87:55:43.5	—	—	—	0.09	0.06	81	20	01:01:39.2	87:56:14.9	—	—	—	0.19	0.08	27	11
01:04:41.3	84:39:14.2	4965	149.9	6.7	0.02	0.03	35	35	01:23:55.4	83:51:18.1	6447	142.9	9.6	0.10	0.04	168	11
01:27:20.1	88:18:29.7	—	—	8.9	0.08	0.02	68.6	6.1	01:51:15.0	87:56:05.0	8397	123.0	9.7	0.08	0.02	83.6	8.0
01:58:03.4	88:35:40.1	8846	234.2	7.9	0.04	0.01	169.8	5.0	02:04:06.6	85:47:01.6	9504	166.4	9.2	0.01	0.04	0	—
02:05:56.2	86:58:25.3	9614	178.9	8.1	0.03	0.05	41	—	02:12:42.1	87:43:20.6	41951	—	10.3	0.77	0.06	76.8	2.0
02:18:11.6	83:36:06.6	10623	131.2	6.4	0.02	0.02	83	35	02:20:57.6	85:46:34.6	10800	174.2	7.0	0.02	0.01	71	14
02:37:39.4	88:12:42.8	4628671	—	10.7	0.37	0.06	159.0	4.8	02:39:42.1	88:30:32.2	11980	154.1	8.1	0.03	0.01	161	13
02:37:56.5	87:27:52.3	12003	770.0	9.9	0.07	0.08	180	32	02:38:23.2	83:21:14.5	12175	233.1	9.6	0.05	0.02	3.6	9.7
02:39:04.3	83:52:20.4	12232	197.2	6.7	0.03	0.04	78	43	02:41:43.2	85:05:48.2	12410	114.3	8.6	0.23	0.03	32.0	3.2
02:48:48.8	85:50:08.6	12952	154.6	7.8	0.03	0.01	84.5	9.3	02:55:13.8	88:41:48.4	4628201	—	8.8	0.04	0.03	73	27
03:07:19.9	87:03:35.5	14285	157.2	7.8	0.02	0.01	2	23	03:13:30.7	82:56:11.3	14859	196.5	7.1	0.03	0.02	88	24
03:37:20.5	88:17:18.9	4628941	—	10.5	0.23	0.07	13.0	8.6	03:38:32.6	86:25:42.1	16754	147.0	9.0	0.19	0.04	69.0	5.3
03:48:26.5	86:36:21.1	4624631	—	10.3	0.38	0.06	71.5	4.3	03:52:07.4	87:55:23.2	17673	117.8	8.8	0.04	0.02	1	14
03:58:59.4	85:16:41.2	18436	207.5	9.2	0.07	0.02	10.2	7.5	05:30:24.0	88:19:27.2	4629801	—	10.7	0.46	0.10	177.5	6.2
05:46:50.8	85:40:17.3	27015	144.9	6.7	0.14	0.03	0.7	6.8	06:18:53.3	88:07:40.1	29457	101.3	10.6	0.10	0.03	35.8	7.5
07:36:37.2	88:37:04.1	36324	152.2	9.2	0.15	0.01	165.4	2.6	07:46:01.2	88:26:33.3	37247	211.4	10.0	0.16	0.05	158.5	9.1
08:18:35.5	87:39:53.5	40335	177.6	9.1	0.10	0.05	169	12	09:09:47.6	88:17:12.1	44563	147.5	9.9	0.11	0.03	177.5	7.5
09:27:07.4	88:31:55.9	45919	125.6	7.1	0.09	0.03	1.6	8.6	09:40:01.7	88:28:22.3	47044	138.1	9.6	0.07	0.05	12	18
09:59:52.4	89:31:39.8	47953	147.7	9.0	0.03	0.04	8	33	09:51:23.0	86:48:38.2	48163	153.6	8.3	0.12	0.01	11.5	3.4
10:11:29.2	86:31:58.6	49768	232.6	7.8	0.07	0.03	39	11	10:20:05.8	85:47:04.2	50482	237.5	8.4	0.11	0.04	15.0	9.8
10:51:13.8	87:48:43.8	52908	200.4	8.8	0.08	0.03	30.0	9.7	11:23:01.0	87:35:24.5	55483	205.3	7.5	0.09	0.03	70	11
11:31:50.2	88:42:04.1	56124	153.4	9.5	0.13	0.05	42	11	15:23:24.0	87:24:17.1	75576	130.4	9.1	0.06	0.04	21	17
17:40:42.3	85:39:58.3	86695	114.3	7.6	0.12	0.03	44.0	6.0	17:51:35.5	86:33:25.7	87663	212.8	7.7	0.09	0.03	25	10
20:23:54.5	89:26:11.7	101884	242.1	8.9	0.10	0.05	42	14	20:55:05.4	87:04:00.3	103435	150.4	7.4	0.09	0.04	169	12
21:51:50.0	84:51:55.0	107982	126.3	9.1	0.08	0.03	10	11	22:00:46.6	88:06:56.5	108862	156.2	7.4	0.07	0.03	4	13
22:12:17.2	86:15:54.3	109694	233.6	6.6	0.06	0.02	0	10	22:16:07.2	84:32:54.5	109985	222.7	7.6	0.05	0.03	38	19
22:50:46.7	85:25:13.8	112833	140.1	5.9	0.06	0.03	14	16	23:24:18.4	86:27:58.3	115550	136.1	6.6	0.09	0.02	25.9	7.5
23:36:40.7	83:15:10.1	116496	216.9	7.5	0.08	0.03	0.6	8.5	23:42:34.0	85:31:02.6	116945	242.7	7.7	0.06	0.02	31	10
23:43:09.4	88:23:27.2	117008	241.0	9.0	0.04	0.04	33	29	23:43:57.1	87:24:13.5	117053	141.0	9.5	0.12	0.04	39.8	8.9
23:46:34.1	84:06:08.6	117233	243.3	9.2	0.69	0.02	166.8	1.0	23:47:57.5	85:07:38.3	117350	246.9	7.8	0.06	0.01	35.1	6.5
23:59:57.5	86:45:19.4	118285	193.8	6.8	0.09	0.04	32	12	—	—	—	—	—	—	—	—	—

grains is preferentially perpendicular to the magnetic field, and since the extinction cross section is large for the grains' larger dimension, starlight from background stars acquires a polarization that is aligned with the magnetic field. With visible and near-infrared polarization data, we thus have access to information on the structure of the interstellar magnetic field.

The observations we present here were carried out on the 1.6 m telescope at the Mont-Mégantic Observatory (OMM), Québec, Canada, in March 2010, using an 8.18″ aperture hole and a broadband red filter RG645 (λ_0 = 7660 Å, $\delta\lambda$ = 2410 Å). Polarization data were taken with "Beauty and the Beast" (B&B), a two-channel photoelectric polarimeter, which uses a Wollaston prism, a Pockels cell, and an additional quarter-wave plate (Manset & Bastien 1995). The high sensitivity of the B&B allows to observe lines of sight towards stars with magnitudes in the V band of about $m_V = 9$, with $\sigma_p = 0.03\%$ polarization fraction uncertainty, in about 500 s total integration time (Manset & Bastien 1995). The polarimeter is cooled down with dry ice (replaced every 6 hours or so), down to a temperature of about 200 K. Any given observation is decomposed in 8 steps, corresponding to two measurements (one on the targeted star, one on an empty nearby field) for each one of 4 angles of the polarimeter (0 °, 45 °, 90 °, and 135 °). We obtained polarization data for 65 stars in the Polaris Flare field, with typical integration times of about 1 to 2 minutes per position of the instrument. The empty-sky integration time depends on the weather conditions and was optimized to reach the desired SNR. The raw outputs from the photomultipliers consist in counts which are then used to derive the polarization fraction p and angle ψ. We list the targeted stars in Table 1, giving their coordinates, identifications in the Hipparcos/Tycho catalogues (ESA 1997), distances, magnitudes in the V band, polarization fractions and angles as well as the associated uncertainties. Note that the polarization angles are given in the IAU convention, so that $\psi = 0°$ towards the North Celestial pole, increasing towards the East (see e.g., Planck Collaboration 2015b). The uncertainties are computed in the classical limit $\sigma_\psi = \sigma_p/(2p)$ rad (see, e.g., Planck Collaboration 2015a).

2.2. IRIS

The Polaris Flare is a diffuse, turbulent, and non-starforming molecular cloud (Falgarone et al. 1998; Miville-Deschênes et al. 2010) located near the ecliptic North pole and at intermediate Galactic latitude ($b \simeq 28°$). Estimates of the cloud's distance from the Sun are difficult, although they typically range between D = 100 pc and D = 200 pc (Hily-Blant & Falgarone 2007). For instance, measurements by Zagury et al. (1999) argue for a distance closer to the D = 100 pc mark, based on the fact that a part of the cloud, MCLD123.5+24.9, is a foreground to the Polaris star, whose distance is estimated at $d_P = 132 \pm 8$ pc. On the other hand, Schlafly et al. (2014) find a significantly larger distance $D = 380 \pm 40$ pc using PanSTARRS-1 photometry, but this data excludes regions north of $\delta = 80°$, where all of our stars lie. Consequently, we shall consider here the lower bound $D = 100\,\mathrm{pc}$, in which case all of the stars in our study are in the background of the cloud.

We use the IRIS reprocessing of IRAS data (Miville-Deschênes & Lagache 2005) at $100\,\mu$m, because it is the channel which offers the best contrast for filamentary structures, and the least possible contamination from point sources[2]. The spatial resolution (FWHM) at this frequency is $4.3'$ and we consider a map of the Polaris Flare $12.5°$ across, with $1.5'$ pixels. The physical extent of the map, shown in Fig. 1, is therefore $22\,\mathrm{pc} \times 22\,\mathrm{pc}$ at the assumed distance of 100 pc. One can readily see, before any treatment, that filamentary structures appear across the whole map. That figure also shows the positions and polarization properties of the stars listed in Table 1. In the following statistical analysis, we only keep the 42 stars (marked in blue in Fig. 1) for which the signal-to-noise ratio is $p/\sigma_p > 2$, so that the determination of the polarization angle is accurate (Montier et al. 2015). The angle uncertainty for these stars is at most $13°$.

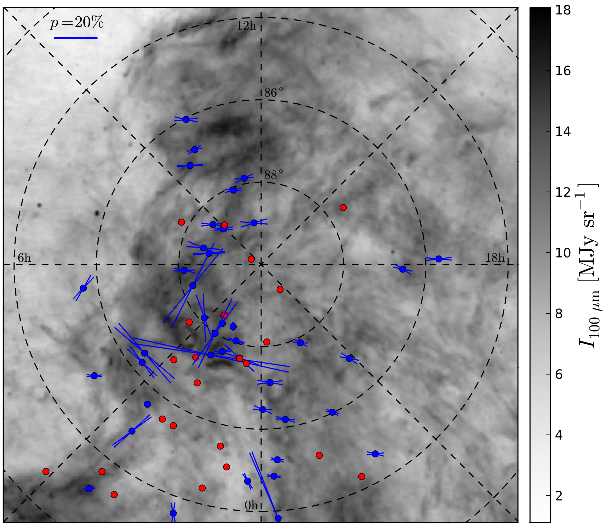

Fig. 1. Positions and polarization properties of the stars listed in Table 1, overlaid on the IRIS $100\,\mu$m map of the Polaris Flare. The field is centered on the North Celestial pole (epoch B1950), and is $12.5°$ across, with $1.5'$ pixels. The polarization is represented (in blue) only for stars for which the signal-to-noise ratio is $p/\sigma_p > 2$: the segments' lengths are proportional to the measured polarization fraction p, and the two segments for each star correspond to angles $\psi \pm \sigma_\psi$, counted positively east from the local north. Stars marked in red have $p/\sigma_p \leqslant 2$ and are not considered in the following analysis.

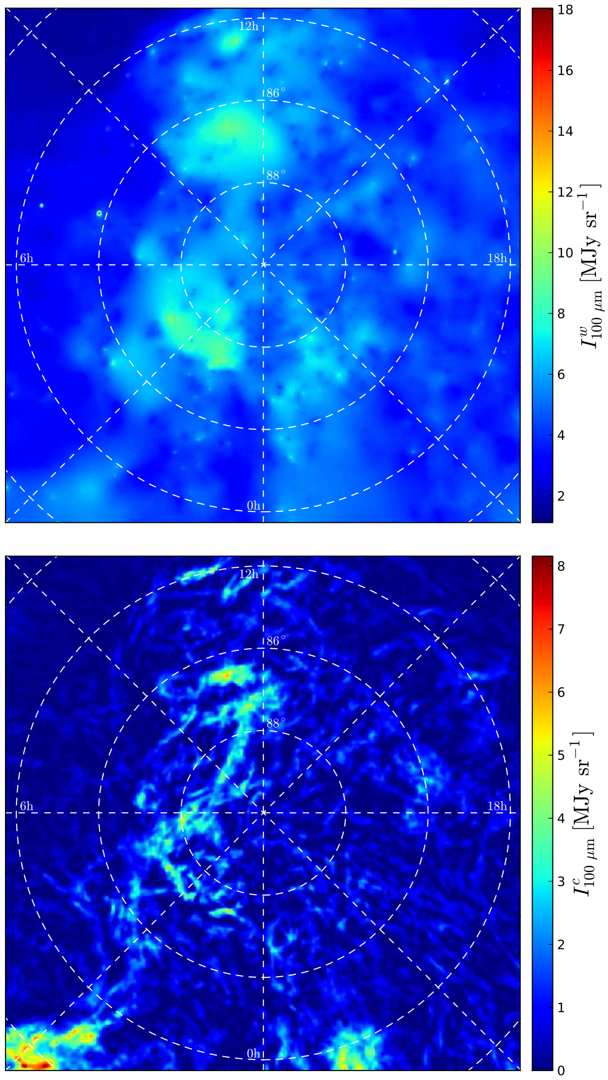

Fig. 2. Wavelet part $I^w_{100\,\mu\mathrm{m}}$ (*top*) and curvelet part $I^c_{100\,\mu\mathrm{m}}$ (*bottom*) of the MCA decomposition of the IRIS $100\,\mu$m map of the Polaris Flare.

3. Extracting filaments from the IRIS $100\,\mu$m map

3.1. MCA decomposition

The filament extraction procedure applied on the IRIS $100\,\mu$m map of dust emission is similar to the one used on *Herschel* maps of IC 5146 by Arzoumanian et al. (2011). The first step is to filter out point sources[3] and enhance the contrast of filamentary structures, which is done with an updated version of MCALab (Fadili et al. 2010). This code implements the Morphological Component Analysis (MCA), an algorithm to find a sparse representation of a given image using two separate dictionaries of functions. In our case, we used the “à trous” wavelet (see, e.g., Starck & Murtagh 1998) and curvelet (Starck et al. 2003) dictionaries. The former is isotropic, so it tends to select point sources at small scales and extended diffuse emission at large scales, while the latter is specifically designed to extract elongated features like curves in the map. The output of the algorithm is a decomposition of the input map $I_{100\,\mu\mathrm{m}}$ in two parts : the isotropic wavelet part $I^w_{100\,\mu\mathrm{m}}$ and the ”filamentary” curvelet part $I^c_{100\,\mu\mathrm{m}}$, which contain respectively 89% and 11% of the total emission. These maps are shown in Fig. 2. The residuals $I_{100\,\mu\mathrm{m}} - \left(I^w_{100\,\mu\mathrm{m}} + I^c_{100\,\mu\mathrm{m}}\right)$ can locally account for up to 10%

[2] We do not use Herschel-SPIRE maps of the Polaris Flare (Miville-Deschênes et al. 2010) because our starlight polarization observations cover a more extended area.

[3] These are maxima in the input field and may lead to the detection of spurious filaments in the subsequent step.

of the total signal, but this only occurs in the most diffuse parts of the map.

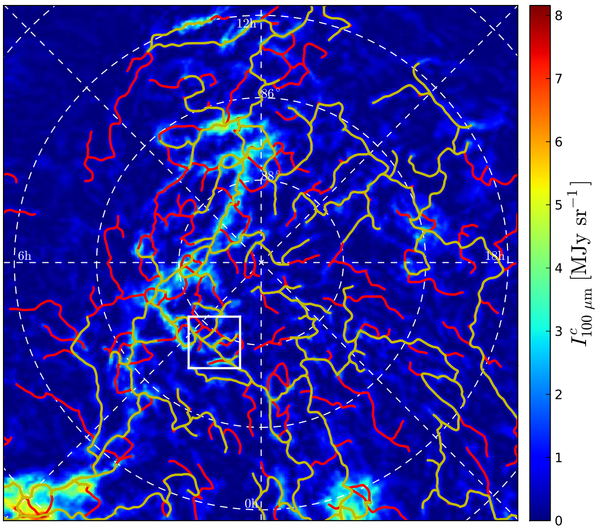

Fig. 3. Illustration of the effect of the persistence threshold. Overlaid on the $I^c_{100\,\mu m}$ map are the skeletons computed with a persistence threshold of $\varpi = 0.5$ MJy sr^{-1} (*union of the red and yellow*) and $\varpi = 1$ MJy sr^{-1} (*yellow only*). In both cases, a smoothing length of 10 pixels is applied. The white box delineates the region shown in Fig. 4.

3.2. Filament extraction with DisPerSE

We apply the `DisPerSE` code (Sousbie 2011) on the curvelet part $I^c_{100\,\mu m}$ of the IRIS map, in order to extract its skeleton, i.e. the network of lines connecting critical points in the input image, following the local gradient $\nabla I^c_{100\,\mu m}$. In our use of `DisPerSE`, we explored two main parameters of the code, the persistence threshold ϖ, and the smoothing length. Filaments are identified by pairs of critical points called persistence pairs, and only retained if the difference between the map values at these points is larger than the chosen persistence threshold. Fig. 3 illustrates the effect of that parameter: as the persistence threshold increases from $\varpi = 0.5$ MJy sr^{-1} to $\varpi = 1$ MJy sr^{-1}, the skeleton is stripped of the less conspicuous filaments.

The second parameter is the smoothing length s, which is described in detail in Sousbie et al. (2009). In summary, each filament is made of waypoints which originally lie either at a pixel corner or at the center of a facet, so that the local orientation of the filament is limited to 8 possible values. For our purpose, smoothing of the skeleton is necessary, and is obtained by a weighted average of these waypoints with their nearest neighbours. Repeating the process s times leads to a smoothing of the filament over a typical scale s pixels. Note that critical points are kept fixed in the process. Fig. 4 illustrates the effect of the smoothing length. One can readily see the raggedness of the skeleton computed with $s = 1$ pixel, compared to the smoothness of the skeleton computed with $s = 10$ pixels.

For our analysis, we have proceeded with a smoothing length $s = 10$ pixels $\simeq 15'$, which is about three beam sizes and provides a continuous distribution of possible orientations for the segments constituting the filaments, as shown in Fig. 5. In

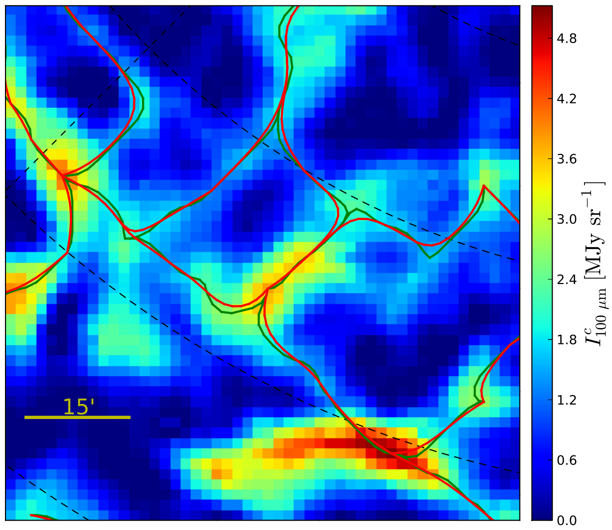

Fig. 4. Illustration of the effect of the smoothing length s. Overlaid on a $1.25° \times 1.25°$ subset of the $I^c_{100\,\mu m}$ are the skeletons computed for the same persistence threshold $\varpi = 0.75$ MJy sr^{-1} and two smoothing lengths, $s = 1$ pixel (in green) and $s = 10$ pixels (in red).

this plot, the orientations ϑ are computed with respect to the local "horizontal" axis in the maps: despite its lack of physical meaning, it is helpful to show the problem of using unsmoothed ($s = 0$) skeletons. The choice of $s = 10$ pixels conversely shows that there is no preferred filament orientation in the Polaris Flare field. We have also chosen a persistence threshold $\varpi = 0.75$ MJy sr^{-1}, which is well above the noise level $\sigma = 0.06 \pm 0.02$ MJy sr^{-1} in the IRIS maps (Miville-Deschênes & Lagache 2005), so the detected filaments cannot be due to noise. We show in Fig. 6 the skeleton computed with these chosen parameters $\varpi = 0.75$ MJy sr^{-1} and $s = 10$ pixels, overlaid on

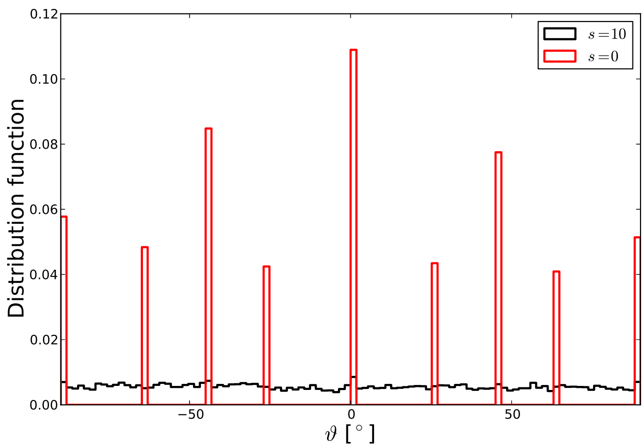

Fig. 5. Distribution functions of the orientations of the segments constituting the skeleton for $s = 0$ (no smoothing, red) and $s = 10$ pixels (black), in both cases for a persistence threshold $\varpi = 0.5$ MJy sr^{-1}. In this plot only, the orientations ϑ are computed with respect to the local "horizontal" axis.

the IRIS 100 μm map (in logarithmic scale) and the starlight polarization data, which we compare to the extracted filamentary structures in the following section.

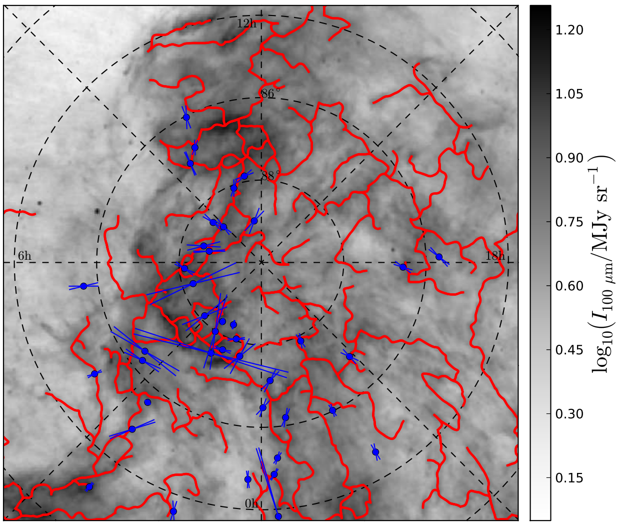

Fig. 6. Skeleton computed with $\varpi = 0.75\,\mathrm{MJy\,sr^{-1}}$ and $s = 10$ pixels (in red), polarization vectors as in Fig. 1 for stars with $p/\sigma_p > 2$, overlaid on the IRIS 100 μm map of the Polaris Flare, in logarithmic scale.

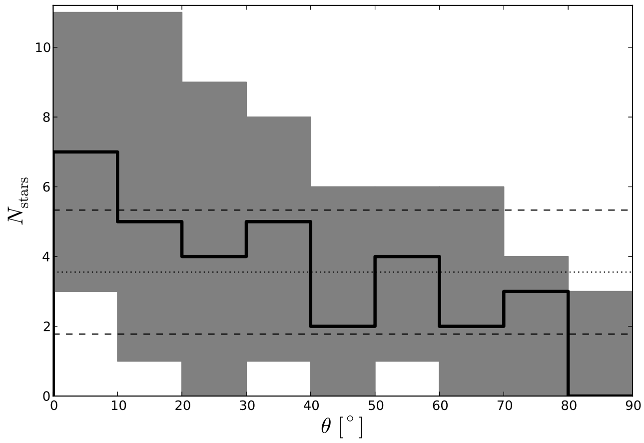

Fig. 7. Distribution of the angles θ between the direction of polarization and the orientation of the skeleton segment closest to the star. The histograms are computed for ψ (black line), and for the set of Monte-Carlo realizations described in the text. The case of a uniform distribution is plotted in thin black dotted lines, with the theoretical statistical standard deviation being plotted in thin black dashed lines.

4. Orientation statistics

To perform this comparison, we are faced with the difficulty of associating a part of a filament to a given star, since the lines of sight towards these are not exactly going through the detected filaments. However, they are often close to one: out of the 42 stars, six lie less than half a beam width (2.1′) away from a skeleton segment, 12 less than one beam width away, 24 less than two beam widths away and 32 less than three beam widths away. The two most isolated stars lie 11.6 and 6.3 beam widths away from a skeleton segment. To keep a reasonably large sample, we have elected to consider the 32 stars whose positions lie less than three beam widths away from the filamentary network[4]. The relative orientation between the filament and the magnetic field at a given star position is then simply computed as the angle between the closest skeleton segment and the direction of polarization (which is also that of the sky projection of the magnetic field). The distribution of these angles is shown as the black line in Fig. 7. To take into account the effect of noise, we ran a set of 50 Monte-Carlo simulations by which, for each star, we replace its measured polarization angle ψ by $\psi + \alpha\sigma_\psi$, where σ_ψ is the uncertainty attached to this measurement and α is a Gaussian-distributed random variable with zero mean and variance unity. The grey area in Fig. 7 shows the span of the resulting distributions of relative angles θ in these Monte-Carlo runs. We observe a deficit of angles close to 90° which is robust with respect to noise, indicating that the magnetic field in the Polaris Flare tends to be aligned with filamentary structures. However, the statistical preference is not completely clear, since the absence of angles in the [80°, 90°] range is only significant at the 2 σ level, with the theoretical statistical standard deviation being $\sigma = 1.78$ for 32 data points in nine bins. Note that the orientations of filamentary structures and of the magnetic field are both three-dimensional quantities, so that the probability distribution function of the angle θ between the corresponding sky projected directions is not fully representative of the three-dimensional distribution of relative angles (Planck Collaboration 2014).

We thus conclude that the observed relative orientations between polarization directions and extracted filaments in the Polaris Flare marginally supports the scenario according to which filaments in the diffuse ISM tend to be aligned with the magnetic field.

5. Summary and conclusions

We have presented new, high-quality starlight polarization data obtained in the Polaris Flare field with the "Beauty and the Beast" polarimeter at Mont-Mégantic Observatory, and have used them to study the relative orientations of the sky projected magnetic field and of nearby filaments of matter traced by the thermal emission from dust at 100 μm observed by IRAS. These filaments are extracted using a two-step process: enhancement via the detection of the curvelet component of the dust emission map, then computation of the skeleton of critical points using the `DisPerSE` code. We find that the distribution of angles θ between the polarization for a given star and the orientation of the nearest filament of matter shows a slight preference towards parallelism, but may also be compatible with a uniform probability distribution function, with few excursions at the 2 σ level. A critical issue to our understanding of the evolution of molecular clouds and the formation of stars is the length scales at which a transition from sub-Alfvénic to super-Alfvénic regimes occurs. It has been proposed that this transition takes place from the outer to the inner parts of molecular clouds (Heyer & Brunt 2012). In the scenario where diffuse filaments feed more mas-

[4] The typical distance between two skeleton segments is larger than this. For instance, the size of the small region enclosed by filaments in the center of Fig. 4 is approximately three beam widths, and one can see in Fig. 3 that it is among the most closely packed set of filaments in the map.

sive ones, sub-Alfvénic motions may be associated with little correlation between the direction of the diffuse filaments with sky-projected magnetic field orientations. In the present work, a weak correlation is found that suggests that the filaments and the magnetic field lines tend to be preferentially aligned. This may be a manifestation of a trans-Alfvénic regime. However, larger statistics are required to put this interpretation on firmer ground. Similar analyses could be performed towards molecular clouds displaying a range of star formation efficiencies, such as the Taurus molecular cloud or the Pipe nebula, for which starlight polarization measurements similar to the ones presented here are available. For instance, the Chameleon Cloud Complex in the Southern hemisphere may be of particular interest because it harbours both star forming and non-star forming clouds (Tsitali et al. 2015).

Acknowledgements. The authors wish to thank K. M. Narasimhan, A. Simon, and P. Didelon.

References

André, P., Di Francesco, J., Ward-Thompson, D., et al. 2014, Protostars and Planets VI, 27
Arzoumanian, D., André, P., Didelon, P., et al. 2011, Astronomy and Astrophysics, 529, L6
Chapman, N. L., Goldsmith, P. F., Pineda, J. L., et al. 2011, The Astrophysical Journal, 741, 21
Crutcher, R. M. 2012, ARA&A, 50, 29
Das, H. K., Voshchinnikov, N. V., & Il'in, V. B. 2010, MNRAS, 404, 265
Davis, Jr., L. & Greenstein, J. L. 1951, ApJ, 114, 206
ESA. 1997, The Hipparcos and Tycho catalogues. Astrometric and photometric star catalogues derived from the ESA Hipparcos Space Astrometry Mission, 1200
Fadili, M. J., Starck, J. L., Elad, M., & Donoho, D. L. 2010, IEEE Computing in Science and Engineering
Falgarone, E., Panis, J. F., Heithausen, A., et al. 1998, Astronomy and Astrophysics, 334, 1145
Hacar, A., Tafalla, M., Kauffmann, J., & Kovács, A. 2013, Astronomy and Astrophysics, 554, 55
Heyer, M. H. & Brunt, C. M. 2012, MNRAS, 420, 1562
Hily-Blant, P. & Falgarone, E. 2007, A&A, 469, 173
Hily-Blant, P., Falgarone, E., & Pety, J. 2008, Astronomy and Astrophysics, 481, 367
Hoang, T., Lazarian, A., & Andersson, B.-G. 2015, Monthly Notices of the Royal Astronomical Society, 448, 1178
Lazarian, A. & Hoang, T. 2007, ApJ, 669, L77
Manset, N. & Bastien, P. 1995, Publications of the Astronomical Society of the Pacific, 107, 483
Men'shchikov, A., André, P., Didelon, P., et al. 2010, Astronomy and Astrophysics, 518, L103
Miville-Deschênes, M.-A. & Lagache, G. 2005, The Astrophysical Journal Supplement Series, 157, 302
Miville-Deschênes, M.-A., Martin, P. G., Abergel, A., et al. 2010, Astronomy and Astrophysics, 518, L104
Montier, L., Plaszczynski, S., Levrier, F., et al. 2015, Astronomy and Astrophysics, 574, A136
Palmeirim, P., André, P., Kirk, J. M., et al. 2013, Astronomy and Astrophysics, 550, 38
Pilbratt, G. L., Riedinger, J. R., Passvogel, T., et al. 2010, Astronomy and Astrophysics, 518, L1
Planck Collaboration. 2011a, Astronomy and Astrophysics, 536, 1
Planck Collaboration. 2011b, Astronomy and Astrophysics, 536, 22
Planck Collaboration. 2011c, Astronomy and Astrophysics, 536, 23
Planck Collaboration. 2014, arXiv.org, 1409.6728
Planck Collaboration. 2015a, Astronomy and Astrophysics, 576, A104
Planck Collaboration. 2015b, Astronomy and Astrophysics, 576, A105
Planck Collaboration. 2015c, Astronomy and Astrophysics, 576, A106
Planck Collaboration. 2015d, arXiv.org, 1502.04123
Schlafly, E. F., Green, G., Finkbeiner, D. P., et al. 2014, The Astrophysical Journal, 786, 29
Soler, J. D., Hennebelle, P., Martin, P. G., et al. 2013, The Astrophysical Journal, 774, 128
Sousbie, T. 2011, Monthly Notices of the Royal Astronomical Society, 414, 350
Sousbie, T., Colombi, S. T., & Pichon, C. 2009, Monthly Notices of the Royal Astronomical Society, 393, 457
Starck, J. L., Donoho, D. L., & Candès, E. J. 2003, Astronomy and Astrophysics, 398, 785
Starck, J.-L. & Murtagh, F. 1998, The Publications of the Astronomical Society of the Pacific, 110, 193
Tauber, J. A., Mandolesi, N., Puget, J. L., et al. 2010, Astronomy and Astrophysics, 520, 1
Tsitali, A. E., Belloche, A., Garrod, R. T., Parise, B., & Menten, K. M. 2015, A&A, 575, A27
Zagury, F., Boulanger, F., & Banchet, V. 1999, Astronomy and Astrophysics, 352, 645